Cooperative large-hysteresis spin-crossover transition in the iron(II) triazolate [Fe(ta)2] metal–organic framework

Maciej Grzywa, Richard Röß-Ohlenroth, Christoph Muschielok, Harald Oberhofer, Artur Błachowski, Jan Żukrowski, Dana Vieweg, Hans-Albrecht Krug von Nidda, Dirk Volkmer

Angaben zur Veröffentlichung / Publication details:

Grzywa, Maciej, Richard Röß-Ohlenroth, Christoph Muschielok, Harald Oberhofer, Artur Błachowski, Jan Żukrowski, Dana Vieweg, Hans-Albrecht Krug von Nidda, and Dirk Volkmer. 2020. "Cooperative large-hysteresis spin-crossover transition in the iron(II) triazolate [Fe(ta)2] metal–organic framework." *Inorganic Chemistry* 59 (15): 10501–11. https://doi.org/10.1021/acs.inorgchem.0c00814.

Cooperative Large-Hysteresis Spin-Crossover Transition in the Iron(II) Triazolate [Fe(ta)$_2$] Metal–Organic Framework

Maciej Grzywa, Richard Röß-Ohlenroth, Christoph Muschielok, Harald Oberhofer, Artur Błachowski, Jan Żukrowski, Dana Vieweg, Hans-Albrecht Krug von Nidda, and Dirk Volkmer*

ABSTRACT: The metal–organic framework [Fe(ta)$_2$] (Hta = 1*H*-1,2,3-triazole) containing Fe(II) ions and 1,2,3-triazolate ligands shows a reversible phase transition while retaining the cubic crystal symmetry and space group $Fd\bar{3}m$ (no. 227). The phase transition between room temperature (RT-[Fe(ta)$_2$]; a = 16.6315(2) Å, V = 4600.39(8) Å^3) and high temperature (HT-[Fe(ta)$_2$]; a = 17.7566(4) Å, V = 5598.6(1) Å^3) phases occurs at a temperature above 290 °C, whereas the phase transition between HT- and RT-[Fe(ta)$_2$] starts at a temperature below 210 °C. Both [Fe(ta)$_2$] polymorphs have identical bond topologies, but they differ by a large increase of the unit cell's volume of 22% for HT-[Fe(ta)$_2$]. The compounds are characterized by powder X-ray diffraction, differential scanning calorimetry, and thermogravimetric analyses. Additionally, Mössbauer spectroscopy, magnetic studies, and the electronic structure of both phases are discussed in detail with respect to the spin-crossover transition from the low-spin (RT-[Fe(ta)$_2$]) to the high-spin phase (HT-[Fe(ta)$_2$]).

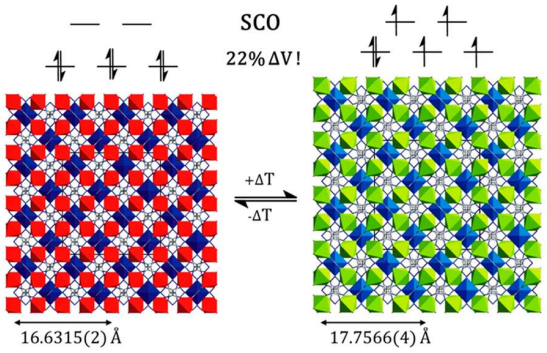

INTRODUCTION

Azoles, poly(azoles), and their derivatives have been used as versatile ligands in constructing coordination polymers.[1] Triazole-based coordination compounds have been extensively investigated since the early 1980s.[2] More than 724 crystal structures containing triazole ligands are found in the Cambridge Structural Database (CSD version 5.41; November 2019).[3] In the past decade, different research groups have spent considerable effort on the synthesis and characterization of coordination frameworks based on triazole ligands and divalent metal ions. Several isostructural MOFs of the type [M(ta)$_2$], composed of M^{II} centers, which are octahedrally coordinated by μ_3-bridging 1,2,3-triazolate ligands, were reported. These materials crystallize in the cubic crystal system within space group $Fd\bar{3}m$ (No. 227). In particular, [Cd(ta)$_2$]·3H$_2$O,[4] [Mn(ta)$_2$], [Co(ta)$_2$], [Zn(ta)$_2$], [Mg(ta)$_2$], and [Fe(ta)$_2$] were investigated.[5] In the first report on [Fe(ta)$_2$], the authors described an intrinsic electrical conductivity of 7.7 × 10^{-5} S/cm,[5] which further increased to 1.0 × 10^{-3} S/cm upon inclusion of I$_2$ into the material by vapor diffusion.[5] Subsequently, this particular framework has become the subject of numerous studies. Sun et al.[6,7] confirmed that within the [M(ta)$_2$] group (M^{II} = Mg, Mn, Fe, Co, Cu, Zn, and Cd), the Fe compound exhibits the highest conductivity. Furthermore, Park et al.[8] have shown that after stochiometric chemical oxidation of the [Fe(ta)$_2$] framework using thianthrenium tetrafluoroborate in MeCN the oxidized materials exhibit drastic enhancements in the electrical conductivity by up to 8 orders of magnitude as compared to stoichiometric [Fe(ta)$_2$], which contains exclusively iron(II) centers. Moreover, [Fe(ta)$_2$(BF$_4$)$_{0.33}$] exhibits an electronic conductivity of 0.3(1) S/cm, which ranks among the highest values for 3D coordination framework materials reported until now. Theoretical aspects of the semiconducting behavior and the electronic structures of [M(ta)$_2$] (M = Zn, Fe, and Ru) compounds have been further explored, based on (hybrid-) density functional theory (DFT) methods.[9]

In our previous work we have shown that in contrast to isostructural compounds of the [M(ta)$_2$]-type, [Cu(ta)$_2$], which contains Jahn–Teller active Cu(II) ions, crystallizes in the tetragonal crystal system.[10] [Cu(ta)$_2$] shows a reversible phase transition from the tetragonal to the cubic crystal system within the temperature range of 120–160 °C. Both [Cu(ta)$_2$] polymorphs have identical bond topologies. α-[Cu(ta)$_2$], as opposed to the high-temperature phase (β-[Cu(ta)$_2$]), shows a strong tetragonal Jahn–Teller distortion of the CuN$_6$(ta) coordination octahedra. Because similar triazolate-based[11–14]

and Hofmann-type[15,16] iron(II)-containing coordination polymers have shown cooperative spin-crossover transitions (SCO), we expected a similar behavior for $[Fe(ta)_2]$. Such spin-crossover compounds have been investigated intensively with respect to their potential usage in memory devices, which demand a wide hysteresis of the SCO.[17−19]

In this paper, we report on our investigations of the wide-hysteresis high-temperature spin-crossover we have discovered in $[Fe(ta)_2]$. This reversible phase transition occurs while retaining the cubic crystal symmetry and space group $Fd\bar{3}m$ (no. 227). The SCO is accompanied by a large increase of the unit cell's volume of nearly 22%. This phase transition is studied by differential scanning calorimetry (DSC) and variable-temperature powder X-ray diffraction (VT-PXRD) measurements. The crystal structures of room-temperature (RT-$[Fe(ta)_2]$) and high-temperature (HT-$[Fe(ta)_2]$) phases were refined by the Rietveld method. The SCO transition was further investigated by Mössbauer spectroscopy and magnetic measurements. In addition, the electronic properties of the low-spin (LS/RT-$[Fe(ta)_2]$) and high-spin (HS/HT-$[Fe(ta)_2]$) phases were studied with all-electron DFT calculations.

RESULTS AND DISCUSSION

Synthesis. $[Fe(ta)_2]$ was prepared in a manner similar to a previously reported procedure.[5] The pink microcrystalline material was obtained by solvothermal reaction of $FeCl_2$ and 1*H*-1,2,3-triazole in DMF in a large batch. All attempts to obtain a sufficiently sized crystal specimen of $[Fe(ta)_2]$ suitable for single-crystal X-ray diffraction study unfortunately failed in our hands although a range of starting materials (different Fe(II) precursors, e.g., iron(II) bromide ($FeBr_2$), iron(II) trifluoroacetate ($Fe(CF_3COO)_2$), iron(II) acetylacetonate ($Fe(acac)_2$), iron(II) acetate ($Fe(OAc)_2$), and ferrocene) and various solvents have been tested (DEF, DMAc, MeOH, EtOH, and propan-2-ol). The largest crystals of $[Fe(ta)_2]$ thus obtained was about 1 μm, resulting from a large-batch synthesis (cf. Figure S9).

PXRD and Physisorption Studies. Phase purity of RT-$[Fe(ta)_2]$ was confirmed by PXRD measurement under ambient conditions. The experimental PXRD pattern is consistent with the simulated one as gleaned from the PXRD (Figure S3). Compound $[Fe(ta)_2]$ exhibits permanent porosity, which was confirmed by argon gas sorption (Figure S4). Prior to measurement, the sample was degassed at 200 °C for 1 h in vacuum. The adsorption data were fitted to the BET equation to give a surface area of 432 m^2g^{-1} (Figure S5), which is in good agreement with data found in the literature (450 m^2g^{-1}).[5]

TGA, VT-PXRD, and DSC Studies. For the characterization of the thermal stability, TGA, VT-PXRD, and DSC experiments were performed. The thermogravimetric profile shown in Figure S2 exhibits the onset of the sample decomposition at ca. 340 °C, although a small weight loss of 2.8% is already observed at this temperature. The VT-PXRD studies have shown that $[Fe(ta)_2]$ is stable up to ca. 350 °C. At 400 °C, the intensity of characteristic Bragg peaks decreases, which relates to decomposition of the framework (see Figure 1a). Heating $[Fe(ta)_2]$ from RT to 350 °C leads to changes of the powder pattern at 300 °C, and the HT-phase is stable up to ca. 350 °C.

Crystallographic Studies. Upon heating the sample of $[Fe(ta)_2]$ to $T > 290$ °C, RT-$[Fe(ta)_2]$ undergoes a reversible first-order endothermic phase transition, without changes of the crystal system, into HT-$[Fe(ta)_2]$, which reverts exothermically to the RT phase upon cooling. Powder X-ray diffraction studies reveal that RT- and HT-$[Fe(ta)_2]$ phases crystallize in the cubic crystal system in the space group $Fd\bar{3}m$ (no. 227). The asymmetric unit contains two iron, two nitrogen, one carbon, and one hydrogen atoms. ORTEP-style plots of the asymmetric units of the RT- and HT-$[Fe(ta)_2]$ phases with atom labels are shown in Figure S1. As shown in Figure 3, RT- and HT-$[Fe(ta)_2]$ comprise coordination units in which the Fe(II) ions are octahedrally coordinated by six tridentate triazolate ligands via nitrogen donor atoms.

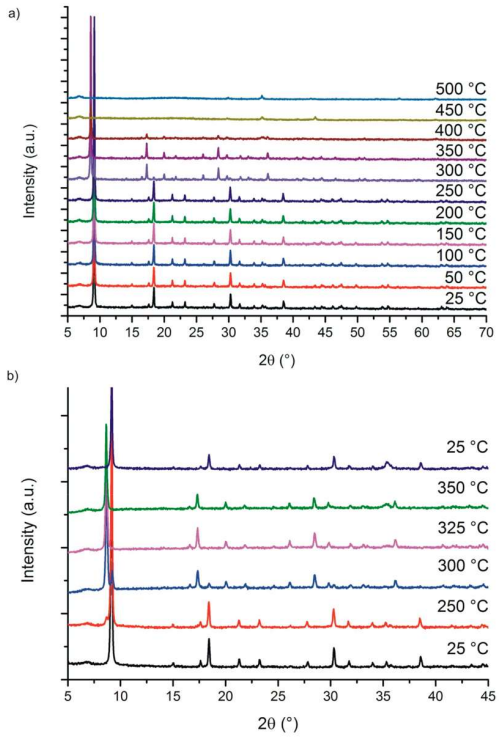

Figure 1. VT-PXRD measurements of $[Fe(ta)_2]$ from room temperature to 500 °C demonstrating the stability of the compound. Temperature steps of 50 °C were applied (a). VT-PXRD measurements of $[Fe(ta)_2]$ from room temperature to 350 °C and cooled to 25 °C showing a reversible phase transition between RT- HT- and RT-$[Fe(ta)_2]$ phases (b).

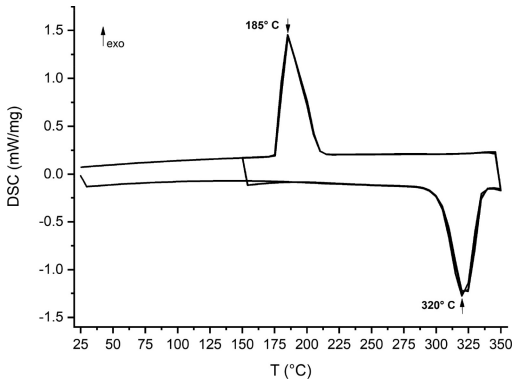

Figure 2. DSC curves for $[Fe(ta)_2]$ registered with a scanning rate of 10 C min^{-1} at heating and cooling (three cycles overlaid on top of each other).

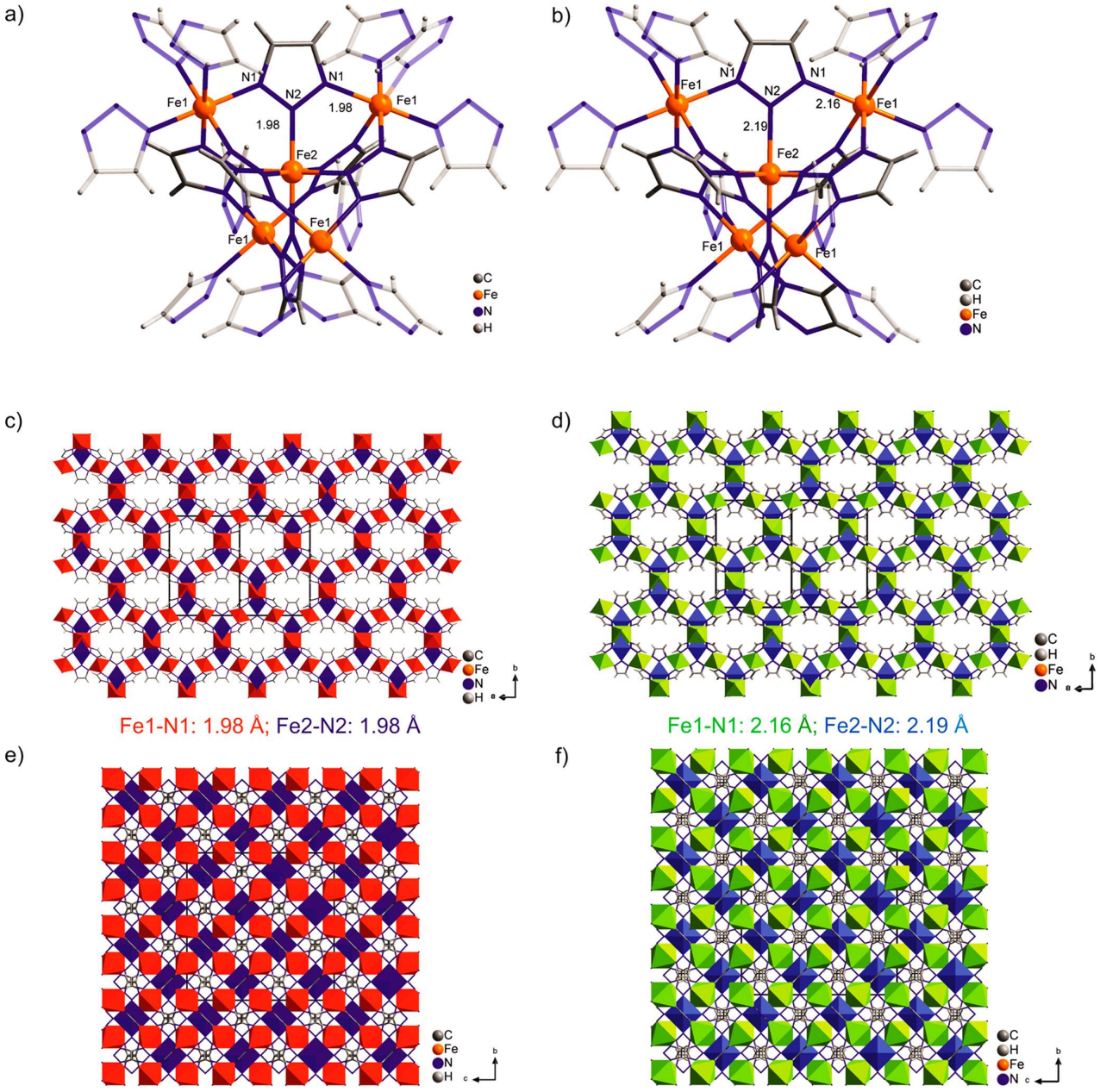

Figure 3. Excerpts of the crystal structures of RT- and HT-[Fe(ta)$_2$] (a) and (b), respectively. Packing diagrams of the crystal structures of RT- and HT-[Fe(ta)$_2$] emphasizing void channels viewed in [110] direction (c, d) and packing diagrams in *a*-direction (e, f). RT-[Fe(ta)$_2$]: red polyhedrons: Fe1{(N1)$_6$}, blue polyhedrons: Fe1{(N2)$_6$}. HT-[Fe(ta)$_2$]: green polyhedrons: Fe1{(N1)$_6$}, blue polyhedrons: Fe1{(N2)$_6$}.

Next, cooling the sample to RT leads to reversible structural changes and the initial powder pattern of the RT phase is retained. Differential scanning calorimetry (DSC) measurements for [Fe(ta)$_2$] were performed in the temperature range of 25−350 °C with a scanning rate of 10 C min^{-1}. Figure 2 shows the temperature dependences of the heat flows (DSC curves) obtained for [Fe(ta)$_2$] on heating and on cooling. Two signals on the DSC curves were registered: During the heating process, an endothermic peak in the temperature range of 290−340 °C is observed, while upon cooling, an exothermic peak between 210−175 °C can be seen. The endothermic maximum relates to the phase transition of the RT to the HT-phase, whereas the exothermic one is connected with the reversible phase transition (i.e., HT to RT-phase).

The [Fe(ta)$_2$] compound consists of Fe$_5$(ta)$_6$ tetrahedra as building units. Four Fe1 ions occupy the vertices of the tetrahedron, while the central Fe2 ion is placed on the geometric center of the coordination unit. In [Fe(ta)$_2$] the Fe(II) ions are placed in FeN$_6$ octahedra. The Fe1 centers, coordinated by N1 atoms are placed at sites with $\bar{3}m$ symmetry, while the Fe2 centers, coordinated by N2 atoms are placed at sites with $\bar{4}3m$ symmetry. The Fe−N distances

indicate that the Fe(II) ions are in the LS state. The thermally induced reversible phase transition of $[Fe(ta)_2]$ from the RT-phase into the HT-phase leads to the SCO of iron ions, which is connected with a large volume expansion of the unit cell (Δa = 1.13 Å), considerably elongating the distances between Fe–N atoms (Δd = 0.18–0.21 Å). This process runs without changing the crystal system and space group symmetry. Cooling the sample below 210 °C leads to the reversible phase transition between HT-$[Fe(ta)_2]$ and RT-$[Fe(ta)_2]$ phases. The crystal structure of $[Fe(ta)_2]$ contains 3D void channels, which are confined by the hydrogen atoms of the triazolate ligands. Void calculations run with the program SQUEEZE[20] reveal that the initial solvent-accessible void volume is 931.7 Å^3, which is 20.3% of the unit cell volume (4600.4 Å^3 for RT-$[Fe(ta)_2]$), and 1621.6 Å^3, which is 29% of the unit cell volume (5598.6 Å^3 for HT-$[Fe(ta)_2]$), respectively for a probe radius of 1.68 Å, corresponding to the approximate van der Waals radius of argon.[21] A dense packing of iron coordination octahedra is observed in the *a*-, *b*-, and *c*-directions (see Figure 3). The network topology of $[Fe(ta)_2]$ can be simplified by considering the imaginary Fe2-centered $Fe2(Fe1)_4$ tetrahedra as 4-connected nodes. The resulting 4-connected diamondlike net can be represented by a 6^6 topological symbol.

Mössbauer Spectroscopy. ^{57}Fe Mössbauer spectra were recorded during heating from 21 °C up to 340 °C and during cooling from 320 °C down to 21 °C for the two absorbers separately, with about 12 h measuring time for each temperature. Additionally, the Mössbauer spectra for another temperature series are shown in Figure S6, and Mössbauer parameters are collected in Table S1. As shown in Figure 4 and Table 1, the main components of spectra taken at RT and upon heating to 280 °C have a shape of narrow pseudosingle line due to the cubic crystallographic structure, which means that both iron sites have the same hyperfine properties (ligand fields) and cannot be distinguished by means of Mössbauer spectroscopy in this temperature range. The spectra have relatively small line widths, small quadrupole splittings of about 0.1 mm/s, and a spectral center shift of δ = 0.38 mm/s (versus α-Fe), typical for a LS divalent iron, although a trivalent iron cannot be excluded on this basis. The obtained Mössbauer parameters at RT are the same as those in literature.[6,8] The same values of the Mössbauer parameters at the beginning and at the end of the measuring series (at 21 °C) verify the full reversibility of the spin-crossover transition. The minor components probably result from some oxidation and subsequent decomposition at high temperature. The spectrum observed at 300 °C in the heating series shows a partial spin transition with about 41% of iron remaining in the previous (LS) state and about 54% of iron transformed to the HS state. Furthermore, one can observe the two subspectra related to Fe(II)-HS with the ratio of about 2:1. It should be kept in mind that the here discussed area contributions of the Mössbauer signals do not necessarily reflect the actual concentrations of the different iron states or sites. Different bond properties of the iron atoms in its lattice position lead to different Mössbauer–Lamb factors (MLF), which give rise to different intensities of the Mössbauer signals. For example, it is known that in the spin-crossover transitions of Fe(II) compounds with strong cooperative interactions, the MLF (and therefore the Mössbauer subspectra areas) could be even up to 20% larger for the LS state than for the HS state.[22] Such a large difference between the MLF for LS and HS iron was

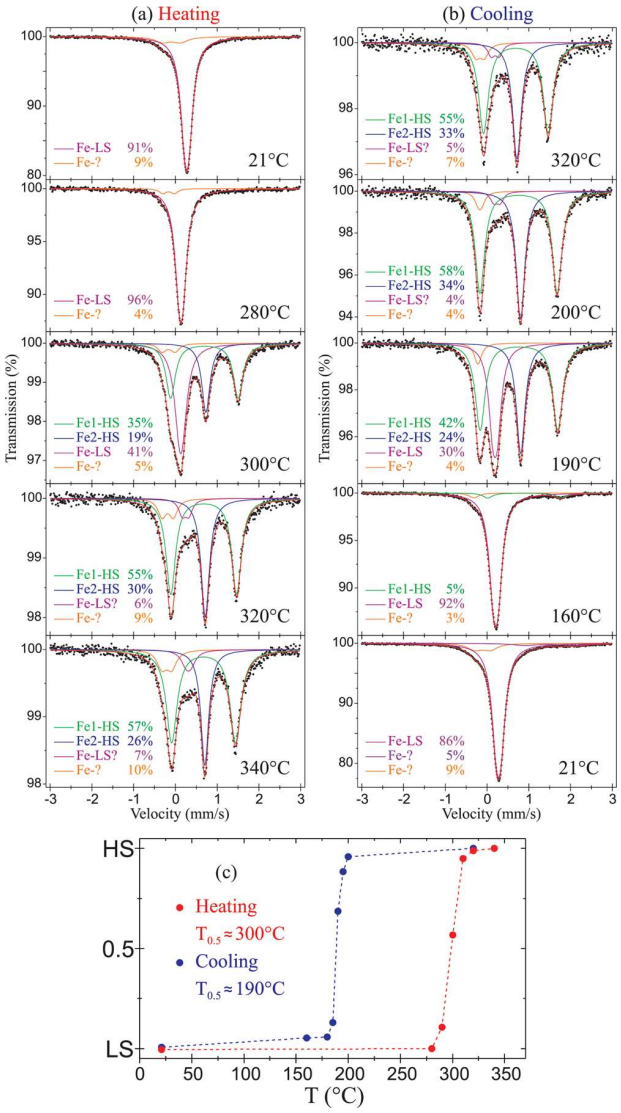

Figure 4. ^{57}Fe Mössbauer spectra for the $[Fe(ta)_2]$ versus temperature series of heating (a) and cooling (b). The measurements were made for two absorbers individually for both series. The contributions of unknown Fe impurities, probably oxidation and/or decomposition products of the $Fe(ta)_2$ are shown with a question mark. (c) Sketch of the SCO thermal hysteresis for the $Fe(ta)_2$ based on the Mössbauer results.

also found in $Fe[(ta)_2]$ and it was estimated based on the temperature dependence of the relative spectral area. It seems that a significant softening of the lattice occurs at the SCO (see the Supporting Information for more details). However, due to unpredictable error of such estimated MLF change and application of Mössbauer spectroscopy to obtain mainly qualitative evidence about the SCO, in this study the area contributions of the Mössbauer spectral components are shown and discussed without correction for the different values of the MLF.

The spectra at 320 and 340 °C in the heating series show the almost-full transition of iron to the HS state and some traces of Fe(II)-LS (probably high temperature decomposition product) and unidentified Fe impurity. The ratio of the two Fe(II)-HS signals remains about 2:1, and at first glance these subspectra

Table 1. ^{57}Fe Mössbauer Parameters for the Spectra Shown in Figure 4

T (°C)	Fe spin state	A (%)[a]	δ (mm/s)[b]	Δ (mm/s)[c]	Γ (mm/s)[d]
		Heating			
21	Fe−LS	91	0.38	0.09	0.14
	Fe-?	9	0.02	0.43	0.33
280	Fe−LS	96	0.24	0.08	0.14
	Fe−?	4	−0.06	0.28	0.10
300	Fe_1−HS	35	0.80	1.62	0.17
	Fe_2−HS	19	0.84		0.13
	Fe−LS	41	0.24	0.07	0.19
	Fe−?	5	−0.05	0.31	0.14
320	Fe_1−HS	55	0.79	1.58	0.17
	Fe_2−HS	30	0.82		0.14
	Fe−LS?	6	0.35	0.16	0.11
	Fe−?	9	−0.08	0.27	0.14
340	Fe_1−HS	57	0.78	1.53	0.21
	Fe_2−HS	26	0.81		0.13
	Fe−LS?	7	0.42	0.11	0.19
	Fe−?	10	−0.10	0.24	0.18
		Cooling			
320	Fe_1−HS	55	0.80	1.55	0.18
	Fe_2−HS	33	0.83		0.15
	Fe−LS?	5	0.30	0.19	0.11
	Fe−?	7	−0.06	0.20	0.15
200	Fe_1−HS	58	0.86	1.85	0.17
	Fe_2−HS	34	0.91		0.15
	Fe−LS?	4	0.35	0.15	0.11
	Fe−?	4	−0.06	0.07	0.11
190	Fe_1−HS	42	0.87	1.86	0.18
	Fe_2−HS	24	0.92		0.15
	Fe−LS	30	0.30	0.11	0.14
	Fe−?	4	−0.11	0.01	0.11
160	Fe_1−HS	5	1.00	1.76	0.18
	Fe−LS	92	0.32	0.11	0.15
	Fe−?	3	−0.21	0.07	0.17
21	Fe−LS	86	0.38	0.10	0.15
	Fe−?	5	1.59	1.15	0.67
	Fe−?	9	−0.01	0.37	0.32

[a] A (%) = relative contribution (subspectrum area). [b] δ (mm/s) = spectral center shift versus room temperature α-Fe. [c] Δ (mm/s) = quadrupole splitting. [d] Γ (mm/s) = absorber line-width (within transmission integral approach). Errors for all values are of the order of unity for the last digit shown.

could be interpreted as related to Fe1-HS and Fe2-HS atoms according to the crystal structure of $[Fe(ta)_2]$ comprising two inequivalent iron sites. The Mössbauer parameters for Fe1-HS and Fe2-HS show almost the same spectral shift of about 0.8 mm/s at the highest temperatures which means that the electron charge density on iron nuclei is almost the same for Fe1 and Fe2 and that both iron are definitely in the divalent HS state. In contrast, the Fe1-HS subspectrum has a quadrupole splitting of about 1.5 mm/s due to a large electric field gradient (EFG) typical for the HS divalent iron. Surprisingly for the Fe2-HS subspectrum, quadrupole splitting is not observed, so it looks like that there is no EFG. This leads to the question: Why is there an unusual single-line Mössbauer spectrum for the HS divalent iron? It is known that the electric field gradient (EFG) is composed of two contributions: (1) the valence electron contribution, which arises from the anisotropic (noncubic) electron distribution in the valence shell of the Fe atoms (anisotropic electron population in the molecular orbitals of the metal centers in the ligand field theory) and (2) the lattice contribution, which arises from a noncubic lattice surrounding. The valence electron contribution for the Fe(II)-HS compounds is generally large, but it could be reduced by lattice contribution because of the opposite signs of the two components. Thus, the lack of EFG for the Fe2-HS could be explained in the following two ways: (1) There is a large lattice contribution to the EFG (large deviation from cubic symmetry) with a value comparable to the valence electron contribution and finally both contributions subtract and null EFG is observed. (2) There is neither the lattice contribution nor the valence electron contribution. The first scenario could be excluded due to the cubic crystallographic symmetry of the $Fe(ta)_2$. The second scenario, with null valence electron contribution to the EFG for the Fe(II)-HS is unusual (or even unknown to our knowledge) for Fe(II)-MOF compounds. According to ligand field theory for the octahedron with O_h symmetry there is a quintet $^5T_2$ ground state with five degenerate orbitals that split into e_g and t_{2g} orbitals with the six electrons of the d^6 configuration of Fe(II) accommodated according to Hund's rule of maximum spin multiplicity. The null EFG could emerge if the four t_{2g} electrons would be uniformly distributed over the three degenerate orbitals of the cubic subgroup and thus preventing the observation of a splitting due to a Jahn−Teller effect, which would lead to distortion of the octahedron. The lack of the EFG suggests that the Fe2 site keeps the O_h symmetry in the HS state with lack of a Jahn−Teller distortion at least in the static case of this effect. It should be kept in mind that the Mössbauer signal is measured in the time window of the excited resonant nuclear level lifetime and the nuclear quadrupole moment precession period (∼100 and ∼10 ns for ^{57}Fe, respectively) and for the rapid oscillations of bonds the EFG could be time-averaged to a zero value. Such effect has been proposed as the reason for the unusual single-line Mössbauer spectrum with null EFG for Fe(II)-HS in the hexaammine ferrous complexes containing the $[Fe(NH_3)_6]^{2+}$ cation.[23,24]

Thus, a possible answer to the raised question may be a temperature-dependent dynamic effect such as the dynamic Jahn−Teller distortion with the rapid inversions of the t_{2g} orbitals. The consequence of this is the uncertainty of assignation of the Fe1-HS and Fe2-HS subspectra seen by the Mössbauer spectroscopy to the two inequivalent crystallographic iron sites in the $[Fe(ta)_2]$ (see the Supporting Information for more details).

The Mössbauer spectra in the cooling series show the HS state of Fe(II) down to about 200 °C confirming the wide temperature hysteresis of the SCO transition. The quadrupole splitting Δ for the Fe1-HS subspectrum increases with decreasing temperature from 1.55 mm/s at 320 °C to 1.85 mm/s at 200 °C. This phenomenon is known as a result of temperature-dependent population of the valence orbitals, i.e., low-lying excited electron levels depopulate on lowering of the temperature, thereby enforcing the deviation of the charge distribution from cubic symmetry and increasing the valence electron contribution to the EFG. However, the Fe2-HS subspectrum remains a narrow single line without any quadrupole splitting. The spectrum at 190 °C upon cooling shows partial spin transition with about 66% of iron remaining in previous HS state and about 30% of iron transformed to the LS state. At 160 °C, only traces of Fe(II)-HS are still visible, but finally the spectrum at 21 °C shows the LS iron (with some

traces of impurity and probably decomposition product). The fact that the same values of the Mössbauer parameters (at 21 °C) assigned to LS-Fe(II) are retained after a full heating and cooling cycle confirms the full reversibility of the SCO transition.

Additionally, ^{57}Fe Mössbauer spectra of the $[Fe(ta)_2]$ were recorded in a liquid nitrogen cryostat from −196 to 22 °C. The pseudosingle line with small and constant quadrupole splitting of about 0.1 mm/s for the LS-Fe(II) was observed for all these temperatures with spectral center shift δ (including temperature-dependent second-order Doppler shift) shown in Figure 5. A relatively very high value of the Debye temperature Θ_D =

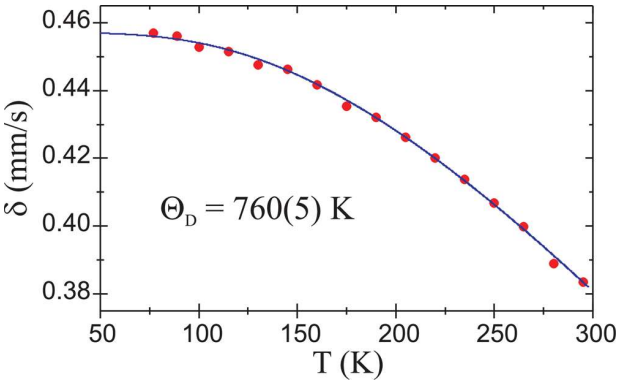

Figure 5. Debye temperature Θ_D = 487(5) °C for the $[Fe(ta)_2]$ in LS state calculated from the low-temperature dependence of the ^{57}Fe Mössbauer spectral center shift δ. The solid line represents the best-fit to the experimental data in terms of the Debye model for the phonon spectrum.

487(5) °C calculated on this basis indicates the large rigidity of the LS iron bindings in the $[Fe(ta)_2]$. Such a high value of Θ_D is rather typical for metallic systems than for metal−organic complexes, but it should be kept in mind that some lattice softening occurs at the SCO as seen by the MLF change (see the Supporting Information for more details).

Magnetic Susceptibility. Figure 6 shows the temperature dependence of the molar magnetic susceptibility of $[Fe(ta)_2]$ above room temperature in a $\chi_M T$ plot. With $\chi_M T$ = 1 emu K/mol, the susceptibility at room temperature is higher than expected for a pure Fe(II) LS (S = 0) compound, but still significantly lower as if all Fe(II) ions were already in the HS (S = 2) state, i.e., at $\chi_M T$ = 9 emu K/mol indicated as dashed line. Similar observations are described in literature, were material defects, introduced by grinding or fast precipitation, are shown to increase the susceptibility of the LS phase.[25−28] This observation further confirms the Mössbauer data, showing mainly LS iron(II) and some unknown impurities. Upon heating from room temperature, the $\chi_M T$ value of $[Fe(ta)_2]$ significantly increases between 280 and 297 °C up to 7 emu K/mol. Subsequently, on cooling, the $\chi_M T$ value first reaches a plateau and then rapidly decreases again between 200 and 180 °C down to about 2 emu K/mol, not completely closing the hysteresis loop.

This irreversible increase of the susceptibility, while passing the hysteresis loop up and down, can be attributed to the formation of small amounts of a ferromagnetic impurity. Note that heating the sample above 297 °C gave rise to much higher irreversible ferromagnetic contributions. For this reason, it was not possible to obtain reliable susceptibility data at higher

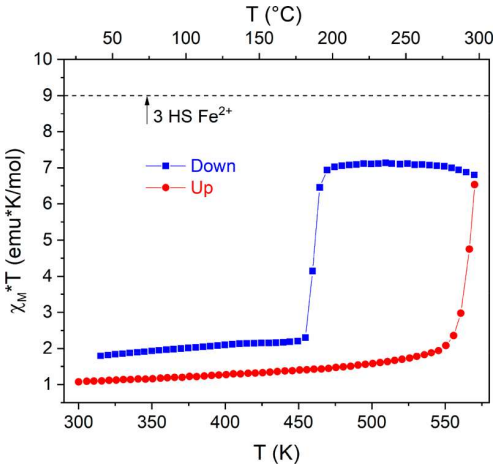

Figure 6. Temperature dependence of the molar magnetic susceptibility of $[Fe(ta)_2]$ in $\chi_M T$ representation taken on increasing (red circles) and decreasing (blue squares) temperature based on the $Fe_3C_{12}H_{12}N_{18}$ sum formula.

temperatures. Nevertheless, the temperature hysteresis observable in the present data is in fair agreement with the results of DSC measurements and of Mössbauer spectroscopy. The increase of the susceptibility upon heating above 280 °C is the clear fingerprint of the LS to HS transition of the Fe ions. On cooling below 200 °C they return to the LS state. Due to the fact, that we approached the LS to HS transition only carefully from below, the spin cross over is not complete but only partially realized.

We also investigated the low-temperature regime of the magnetic susceptibility down to helium temperature (Figure S10). For the Fe^{2+} LS (S = 0) state one would expect an approximately temperature-independent van Vleck type contribution from the low-lying excited states. Indeed, the data exhibit such a contribution of the order of 10^{-3} emu/mol, but in addition, a Curie contribution shows up, very similar to that of $[Fe(ta)_2(BF_4)_x]$, where oxidized samples (x > 0) contain a certain amount of Fe^{3+} giving rise to mixed valence, electrical conductivity, and nonzero spin.[8] This idea is supported by the observation that in $[Fe(ta)_2]$ the strength of this contribution significantly depends on the preparation route. For the present sample, the obtained Curie constant would correspond to 6.6% of Fe^{3+} (spin S = 5/2, g = 2). Moreover, our preliminary electron spin resonance measurements detect resonance signals typical for trivalent iron. However, deeper systematic magnetic investigations are needed to unravel the origin and influences on the magnetic susceptibility of the LS $[Fe(ta)_2]$.

DFT Studies of LS- and HS-$[Fe(ta)]_2$. We model the observed RT- and HT-phases of $[Fe(ta)_2]$ using optimized primitive unit cells of the compound. To distinguish them from the observed-phases, we call them the LS structure which models the RT-phase and two HS structures which model possible spin states in the HT-phase.

A standard DFT calculation without any spin constraints yields the LS structure with a total spin moment of zero with respect to the cell; all formal Fe(II) ions individually assume a LS state. For the HS structures, we therefore use spin constraints. They are chosen such that each iron center assumes a HS state. The two structures we study then only differ in the alignment of the individual spin moments within

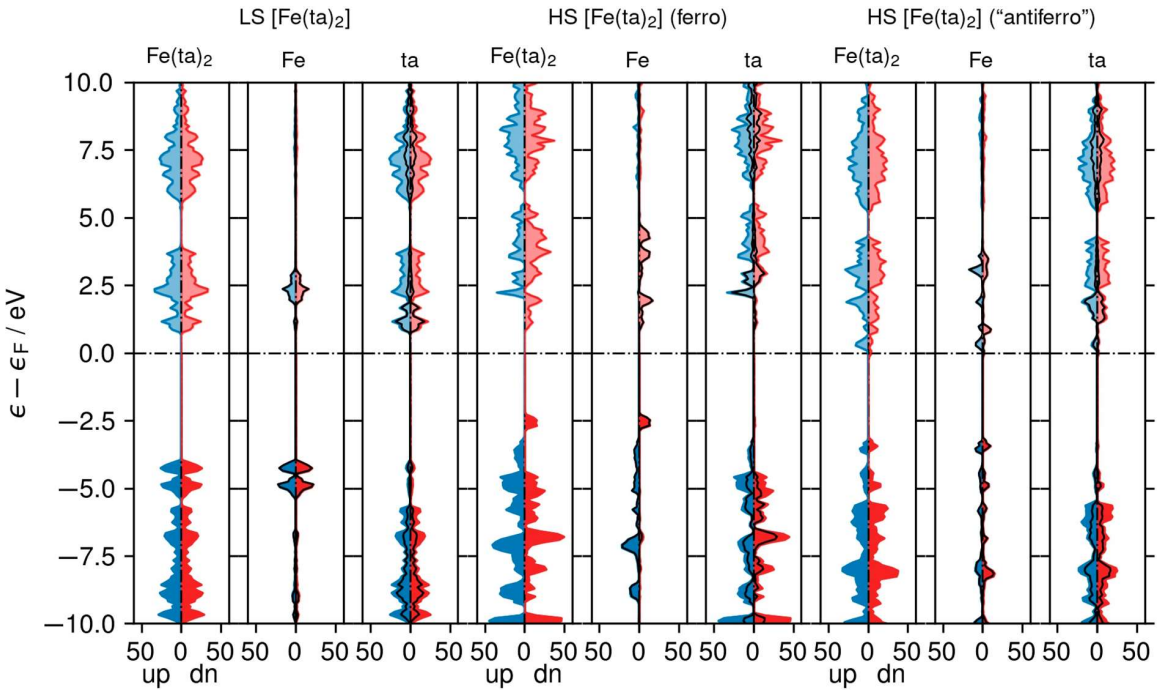

Figure 7. Total DOS and pDOS of $[Fe(ta)_2]$. For the LS-phase (left), the HS-phase in the ferromagnetic configuration (middle) and the HS-phase in the "antiferromagnetic" configuration (right). On each vertical axis, the corresponding (partial) density of states for each spin channel, up (up) and down (dn) respectively, is shown. The black lines show either the pDOS for the Fe d-states or the N p-states, respectively. The energy zero on the *y* axis is set to the Fermi level which FHI-aims adjusts such that the number of electron states equals the number of hole states.

the unit cell. This way, we can prepare both a "ferromagnetically" ordered primitive $[Fe(ta)_2]$ cell in which all HS Fe(II) moments are aligned and multiple "antiferromagnetically" ordered cells, in which three of the iron centers have antiparallel spin moments. Of the latter structures, we focus on a single, representative one here (see the Supporting Information for a sketch of the chosen spin structure).

The LS structure gives an approximation of the definite ground-state of $[Fe(ta)_2]$ and the "ferromagnetic" HS structure gives an upper boundary to the spin effects observed in the HT-phase. Thus, we concentrated our investigation mostly on these two structures, omitting an in-detail study of the "antiferromagnetically" ordered ones. For the LS structure, the Fe centers are not distinguishable by their spin as each center shows a total spin moment of zero. By symmetry we can distinguish the central iron ions of the cluster (Fe1) from the ones on the vertices (Fe2), which tetrahedrally surround the central iron ion. The members of each group of iron centers are indistinguishable among themselves based on Mulliken charges. This behavior is reflected in the density of states (DOS) of the LS structure which shows symmetric spin channel data (Figure 7).

In the HS structure, the individual iron centers of the "ferromagnetic" structure show a spin moment of approximately 4, as obtained through Mulliken charge analysis. Structurally, the HS configuration shows a severely dilated cell ($a = b = c = 1.25$ nm for the HS ferromagenetic configuration and $a = b = c = 1.24$ nm for the antiferromagentic one) compared to the LS ground state ($a = b = c = 1.17$ nm). This comes at a cost of the HS structure being in total 2.79 eV (0.47 eV per metal center in the simulation cell) higher in energy than the LS state. We note that our approach ensures that the HS structure is an energy minimum for the HS electronic structure. The DOS plots of the different spin channels are not congruent, indicating the HS configuration of the Fe centers (Figure 7). From the projected DOS (pDOS), we see that both valence and conduction band edges in the HS state predominantly consist of metal d states, as already observed for similar HS-triazolates by Sun and co-workers.[6]

When considering the "antiferromagnetically" ordered HS structure, the DFT converges to a configuration with three HS moments with $N_{up} - N_{down} \approx +4$ and three HS moments with $N_{up} - N_{down} \approx -4$ on the six iron centers in the cell (cf. Figures 7 and S11). Energetically, this structure is almost degenerate with respect to the "ferromagnetically" ordered all-HS structure discussed before, with an energy difference to the LS structure of 2.81 eV. Accounting for the complexity of the observed electronic states, we validated our results for all three spin-states using the CRYSTAL code with set symmetry constraints to rule out any artifacts in the symmetry unconstrained FHI-aims results. Both codes yielded comparable band gaps and DOSs, which is why we only show FHI-aims results here.

CONCLUSIONS

The high-temperature phase transition of $[Fe(ta)_2]$ was investigated and characterized in detail. VT-PXRD and DSC measurements clearly showed the occurrence of a reversible first-order endothermic-phase transition upon heating above 290 °C, which relaxes exothermically into the initial phase after cooling below 216 °C. The structures of the RT- and HT-phases were refined by the Rietveld method and show no change of the cubic crystal system and the $Fd\bar{3}m$ (No. 227) space group, but they yet have a large increase of the unit cell parameter (RT-$[Fe(ta)_2]$: $a = 16.6315(2)$ Å, $V = 4600.39(8)$ Å^3 and HT-$[Fe(ta)_2]$: $a = 17.7566(4)$ Å, $V = 5598.6(1)$Å^3),

which causes the materials volume to increase by nearly 22%. The nature of this cooperative-phase transition is attributed to a low to high SCO of the iron centers as revealed by Mössbauer spectroscopy and magnetic susceptibility measurements. LS- and HS-$[Fe(ta)_2]$ phases were additionally investigated with regard to their electronic structures, employing DFT methods, the latter clearly indicating an all LS RT-$[Fe(ta)_2]$ phase.

On the basis of DSC measurements the temperature range at which the hysteresis of the SCO transition occurs is about 135 °C, while magnetic measurements provides about 106 °C. The temperature range is higher in comparison to the reported in the literature compounds like $[FeL(HIm)_2]$ (70 °C; L = diethyl (*E*,*E*)-2,2′-[1,2-phenylenebis(iminomethylidyne)]-bis-[3-oxobutanoate]) or $[Fe(pyrazine)[M(CN)_4]\}$ (60 °C; M = Pd and Pt).[29−31] Although the transition occurs at high temperature, the porosity of this compound allows for investigation of the influences on the SCO from postsynthetic modifications or interaction with guest molecules similar to reports found in literature.[12,29,32]

EXPERIMENTAL SECTION

General Information. Commercially available reagents of analytical grade were used as received without further purification. $FeCl_2$ (99.99%) was purchased from Sigma-Aldrich. 1*H*-1,2,3-Triazole was degassed and stored under argon atmosphere. Fourier transform infrared (FTIR) spectra were recorded with ATR in the range 4000−400 cm^{-1} on a Bruker Equinox 55 FT-IR spectrometer. The following indicators are used to characterize absorption bands: strong (s), medium (m), and weak (w). Elemental analysis was measured with a Vario EL III instrument from Elementar Analysensysteme GmbH. Thermogravimetric analysis (TGA) was performed with a TGA Q500 analyzer in the temperature range of 25−700 °C in flowing nitrogen at a heating rate of 5 °C min^{-1}. Argon adsorption isotherms were measured with a Quantachrome Autosorb-I ASI-CP-8 instrument in the range of $5.00 \times 10^{-5} \leq p/p_0 \leq 1.00$ at −196 °C. Adsorbed gas amounts are given in $cm^3\ g^{-1}$ [STP], where STP = 101.3 kPa and 0 °C. Prior to measurements, the sample was heated at 200 °C for 1 h in high vacuum in order to remove rest of occluded solvent molecules. Ambient-temperature PXRD patterns were measured with a Seifert XRD 3003 TT diffractometer equipped with a Meteor 1D detector operated at 40 kV, 40 mA, Cu Kα (λ = 1.54247 Å) with a scan speed of 1 s per step and a step size of 0.02° in 2θ. The VT-PXRD data were collected in the 2θ range of 5−60° with 0.02° steps, with a with an Empyrean (PANalytical) diffractometer equipped with Bragg−Brentano^{HD} mirror, PIXcel^{3D} 2 × 2 detector and XRK 900 reactor chamber. Temperature program between measurements comprised the following: heating rate (0.5 °C s^{-1}), then 10 min isothermal. The patterns were recorded in the 4−50° = 2θ range, with 1 step per 1 s and an angular step width of 0.026° in 2θ. DSC measurements were carried out using NETZSCH DSC 204F1 instrument.

Synthesis. $[Fe(ta)_2]$ was synthesized using common Schlenk line techniques under argon atmosphere by a modified procedure similar to literature.[5] $FeCl_2$ (0.02 mol, 2.54 g) was dissolved in 25 mL of anhydrous *N*,*N*-dimethylformamide (DMF) in a 50 mL round-bottomed Schlenk flask under an argon atmosphere in an ultrasonic bath. After $FeCl_2$ was completely dissolved in the DMF, 3.48 mL (0.06 mol, 4.15 g,) of 1*H*-1,2,3-triazole were added to the solution. The solution was heated at 120 °C for 20 h in a Heat-ON attachment and subsequently cooled to room temperature. A pink microcrystalline solid was obtained, centrifuged under argon atmosphere, and washed 3 times with 20 mL of dry DMF. The solvent was exchanged 3 times by immersion and centrifugation in 20 mL of dry MeOH for 3 days. Then the solvent was removed, and the sample was dried under vacuum for 6 h at 200 °C to afford a pink/purple powder (2.12g, 55%). FT-IR: 3153 (w), 1590 (w), 1475 (m), 1274 (w), 1228 (w), 1180 (w), 1127 (s), 1001 (m), 780 (s), 728 (m), 495 (m), 418 (w) (cf. Figure S8). Elemental analysis calcd (%): C 25.02, H 2.11, N 43.78. Found: C 24.39, H 2.42, N 43.32.

PXRD Structure Analysis. A microcrystalline sample was deposited in the hollow of a sample holder of XRK 900 reactor chamber, and the measurements for Rietveld refinement were performed under flowing nitrogen at 25 and 300 °C. Diffraction data were collected in the 2θ range of 5−110 with one step per 6.2 s (at 25 °C) and 3 s (at 300 °C), and an angular step width of 0.026° in 2θ. The structure of $[Cd_3(ta)_6]\cdot 6H_2O$[4] was applied as a starting model for the Rietveld refinement of RT- and HT-$[Fe(ta)_2]$ phases. The Rietveld refinement was carried out using the Jana2006 program.[33] Geometric restraints on bond distances for RT-$[Fe(ta)_2]$ were used during the refinement processes. The experimental details and crystal data for RT- and HT-$[Fe(ta)_2]$ are listed in Table 2. The final Rietveld refinement plots are presented in Figure 8.

Table 2. Crystal and Experimental Data for RT- and HT-$[Fe(ta)_2]$

	RT-$[Fe(ta)_2]$	HT-$[Fe(ta)_2]$
chemical formula	$C_{12}\ H_{12}\ Fe_3\ N_{18}$	$C_{12}\ H_{12}\ Fe_3\ N_{18}$
formula weight/g mol^{-1}	575.9	575.9
T/°C	25(2)	300(2)
diffractometer	Empyrean	Empyrean
2θ-range/deg, step size	5−110, 0.026	5−110, 0.026
X-ray source, wavelength/Å	Cu Kα, λ = 1.54178	Cu Kα, λ = 1.54178
crystal system	cubic	cubic
space group	$Fd\bar{3}m$ (No. 227)	$Fd\bar{3}m$ (No. 227)
a/Å	16.6315(2)	17.7566(4)
V/Å^3	4600.39(8)	5598.6(1)
Z, density/g cm^{-3}	8, 1.66	8, 1.37
number of observations	3998	3998
R_p	1.46	1.57
R_{wp}	2.14	2.01
R_{Fobs}	6.65	6.05
R_{Fall}	7.46	12.92

Mössbauer Spectroscopy. ^{57}Fe Mössbauer spectra in the transmission mode were obtained applying water-cooled vacuum oven with the boron nitride sample holder and under dynamic vacuum of about 10^{-6} hPa. Temperature stability during about 12 h measuring time for each temperature was about 0.1 °C. The absorbers in case shown on Figure 4 were prepared mixing 20 mg of $Fe(ta)_2$ sample with the B_4C fine powder. The diameter of the absorbers was 10 mm. Hence, one had 25 mg/cm^2 absorber thickness of the $[Fe(ta)_2]$. A commercial ^{57}Co(Rh) source with activity of about 25 mCi and the source line width 0.106(5) mm/s derived from the fit of the Mössbauer spectrum of the 10 μm thick α-Fe foil was used. Resonant photons of the 14.41 keV line in ^{57}Fe were counted by the LND Kr-filled proportional detector. Measurements were performed by means of the MsAa-4 Mössbauer spectrometer and data were processed by means of the MOSGRAF software within the transmission integral approximation. All spectral shifts are reported versus room temperature α-Fe.

Magnetization Measurements. The magnetization M was measured using a superconducting quantum interference device (SQUID) magnetometer (Quantum Design, MPMS5) working in the temperature range of −271 °C ≤ T ≤ 427 °C and in magnetic fields −5 T ≤ $\mu_0 H$ ≤ 5 T. The temperature dependence of the magnetic susceptibility at a given magnetic field was determined as $\chi = M/H$.

Computational Simulations. For all calculations shown here, we use the all-electron DFT code FHI-aims[34−36] with the standard "light" basis set for each elemental species. The initial structures are obtained by optimizing primitive unit cells, which are generated from experimental PXRD data. For this, the implementation of the BFGS algorithm in FHI-aims with a trust radius of 0.01 eV/Å is used.[37] Furthermore, for all structure relaxations except for the "antiferromagnetic" HS structure, electronic exchange and correlation (XC) are

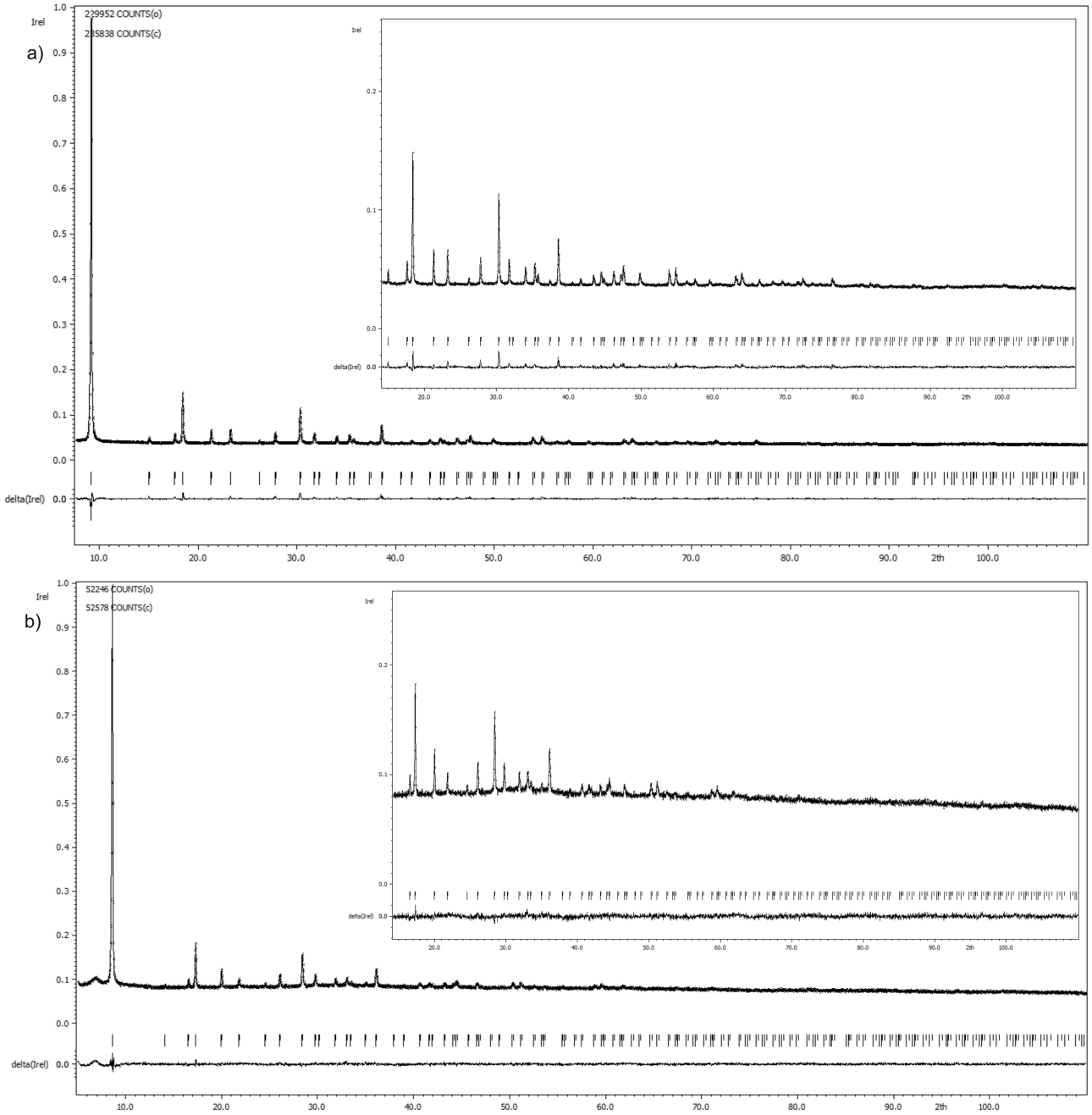

Figure 8. Rietveld refinement plots for RT- and HT-$[Fe(ta)_2]$ (a) and (b), respectively. Dotted and solid lines represent observed and calculated patterns, respectively with peak markers and the difference plot shown at the bottom. PXRD data were collected at 25 °C (a) and 300 °C (b). For clarity, the insets show an expended view in the range 14−110° 2θ.

treated within the generalized gradient approximation (GGA) using the PBE functional and a 2 × 2 × 2 *k*-point grid.[38] For the optimization of the "antiferromagnetic" HS structure, the PBEsol[39] functional was used due to severe convergence problems when using the PBEsol-optimized structure in the subsequent calculation. All other calculations yielding total energies, the density of states (DOS), and projected DOS (pDOS) are performed modeling XC with the PBEsol0 hybrid functional (this is the PBE0 functional based on PBEsol instead of standard PBE).[40] To generate the "ferromagnetically" ordered HS crystal structure of $[Fe(ta)_2]$, we enforce a total spin moment of 24 throughout the unit cell, corresponding to aligned HS configurations of all six formal Fe(II) ions. After optimization, this constraint is lifted for the hybrid functional calculation to yield a stable HS ground-state. For the "antiferromagnetically" ordered structure of $[Fe(ta)_2]$, the same structure as for the "ferromagnetic" case is used. However, the spin constraints are chosen such that three HS Fe(II) centers are antialigned, i.e., they have a spin moment of −4, resulting in a total spin moment of zero for the unit cell.

ASSOCIATED CONTENT

Supporting Information

The Supporting Information is available free of charge at https://pubs.acs.org/doi/10.1021/acs.inorgchem.0c00814.

Asymmetric units, PXRD pattern, Mössbauer spectra, argon adsorption analysis data, IR spectrum, SEM image and low temperature magnetic susceptibility (PDF)

Accession Codes

CCDC 1963572−1963573 contain the supplementary crystallographic data for this paper. These data can be obtained free of charge via www.ccdc.cam.ac.uk/data_request/cif, or by emailing data_request@ccdc.cam.ac.uk, or by contacting The Cambridge Crystallographic Data Centre, 12 Union Road, Cambridge CB2 1EZ, UK; fax: +44 1223 336033.

AUTHOR INFORMATION

Corresponding Author

Dirk Volkmer − *Chair of Solid State and Materials Chemistry, Institute of Physics, University of Augsburg, D-86159 Augsburg, Germany;* orcid.org/0000-0002-8105-2157; Email: dirk.volkmer@physik.uni-augsburg.de

Authors

Maciej Grzywa − *Chair of Solid State and Materials Chemistry, Institute of Physics, University of Augsburg, D-86159 Augsburg, Germany*

Richard Röß-Ohlenroth − *Chair of Solid State and Materials Chemistry, Institute of Physics, University of Augsburg, D-86159 Augsburg, Germany*

Christoph Muschielok − *Theoretical Chemistry, Technische Universität München, D-85747 Garching, Germany*

Harald Oberhofer − *Theoretical Chemistry, Technische Universität München, D-85747 Garching, Germany*

Artur Błachowski − *Institute of Physics, Pedagogical University, 30-084 Kraków, Poland*

Jan Żukrowski − *Academic Center for Materials and Nanotechnology, AGH University of Science and Technology, 30-059 Kraków, Poland*

Dana Vieweg − *Experimental Physics V, Center for Electronic Correlations and Magnetism, Institute of Physics, University of Augsburg, D-86159 Augsburg, Germany*

Hans-Albrecht Krug von Nidda − *Experimental Physics V, Center for Electronic Correlations and Magnetism, Institute of Physics, University of Augsburg, D-86159 Augsburg, Germany*

Complete contact information is available at: https://pubs.acs.org/10.1021/acs.inorgchem.0c00814

Author Contributions

The manuscript was written through contributions of all authors. All authors have given approval to the final version of the manuscript.

Notes

The authors declare no competing financial interest.

ACKNOWLEDGMENTS

Financial support by the Deutsche Forschungsgemeinschaft (DFG) via SPP 1928 COORNETs: Coordination Networks: Building Blocks for Functional Systems is gratefully acknowledged. H.-A.K.v.N. acknowledges the partial support by the DFG via the Transregional Collaborative Research Center TRR 80 "From Electronic Correlations to Functionality" (Augsburg, Munich, Stuttgart)

REFERENCES

(1) Aromí, G.; Barrios, L. A.; Roubeau, O.; Gamez, P. Triazoles and tetrazoles: Prime ligands to generate remarkable coordination materials. *Coord. Chem. Rev.* **2011**, *255*, 485−546.

(2) Triazoles 1, 2, 4. In *Chemistry of Heterocyclic Compounds v. 37*; Temple, C., Montgomery, J. A., Eds.; Wiley: New York, 1981.

(3) Groom, C. R.; Bruno, I. J.; Lightfoot, M. P.; Ward, S. C. The Cambridge Structural Database. *Acta Crystallogr., Sect. B: Struct. Sci., Cryst. Eng. Mater.* **2016**, *72*, 171−179.

(4) Zhou, X.-H.; Peng, Y.-H.; Du, X.-D.; Zuo, J.-L.; You, X.-Z. Hydrothermal syntheses and structures of three novel coordination polymers assembled from 1,2,3-triazolate ligands. *CrystEngComm* **2009**, *11*, 1964−1970.

(5) Gándara, F.; Uribe-Romo, F. J.; Britt, D. K.; Furukawa, H.; Lei, L.; Cheng, R.; Duan, X.; O'Keeffe, M.; Yaghi, O. M. Porous, conductive metal-triazolates and their structural elucidation by the charge-flipping method. *Chem. - Eur. J.* **2012**, *18*, 10595−10601.

(6) Sun, L.; Hendon, C. H.; Park, S. S.; Tulchinsky, Y.; Wan, R.; Wang, F.; Walsh, A.; Dincă, M. Is iron unique in promoting electrical conductivity in MOFs? *Chem. Sci.* **2017**, *8*, 4450−4457.

(7) Sun, L.; Campbell, M. G.; Dincă, M. Electrically Conductive Porous Metal-Organic Frameworks. *Angew. Chem., Int. Ed.* **2016**, *55*, 3566−3579.

(8) Park, J. G.; Aubrey, M. L.; Oktawiec, J.; Chakarawet, K.; Darago, L. E.; Grandjean, F.; Long, G. J.; Long, J. R. Charge Delocalization and Bulk Electronic Conductivity in the Mixed-Valence Metal-Organic Framework $Fe(1,2,3\text{-triazolate})_2(BF_4)_x$. *J. Am. Chem. Soc.* **2018**, *140*, 8526−8534.

(9) Muschielok, C.; Oberhofer, H. Aspects of semiconductivity in soft, porous metal-organic framework crystals. *J. Chem. Phys.* **2019**, *151*, 015102.

(10) Grzywa, M.; Denysenko, D.; Hanss, J.; Scheidt, E.-W.; Scherer, W.; Weil, M.; Volkmer, D. CuN_6 Jahn-Teller centers in coordination frameworks comprising fully condensed Kuratowski-type secondary building units: Phase transitions and magneto-structural correlations. *Dalton Trans.* **2012**, *41*, 4239−4248.

(11) Roubeau, O. Triazole-based one-dimensional spin-crossover coordination polymers. *Chem. - Eur. J.* **2012**, *18*, 15230−15244.

(12) Bao, X.; Liu, J.-L.; Leng, J.-D.; Lin, Z.; Tong, M.-L.; Nihei, M.; Oshio, H. Spin crossover versus low-spin behaviour exhibited in 2D and 3D supramolecular isomers of $[Fe^{II}(2,4\text{-bpt})_2]$·Guest. *Chem. - Eur. J.* **2010**, *16*, 7973−7978.

(13) Bao, X.; Guo, P.-H.; Liu, J.-L.; Leng, J.-D.; Tong, M.-L. Crystalline-state cis-to-trans transformation of a two-dimensional spin-crossover system. *Chem. - Eur. J.* **2011**, *17*, 2335−2339.

(14) Bao, X.; Leng, J.-D.; Meng, Z.-S.; Lin, Z.; Tong, M.-L.; Nihei, M.; Oshio, H. Tuning the spin states of two apical iron(II) ions in the trigonal-bipyramidal $[(Fe^{II}((\text{-bpt})_3{>}_2Fe^{II}_3((\text{-O})]^{2+}$ cations through the choice of anions. *Chem. - Eur. J.* **2010**, *16*, 6169−6174.

(15) Ni, Z.-P.; Liu, J.-L.; Hoque, M. N.; Liu, W.; Li, J.-Y.; Chen, Y.-C.; Tong, M.-L. Recent advances in guest effects on spin-crossover behavior in Hofmann-type metal-organic frameworks. *Coord. Chem. Rev.* **2017**, *335*, 28−43.

(16) Muñoz, M. C.; Real, J. A. Thermo-, piezo-, photo- and chemo-switchable spin crossover iron(II)-metallocyanate based coordination polymers. *Coord. Chem. Rev.* **2011**, *255*, 2068−2093.

(17) Senthil Kumar, K.; Ruben, M. Emerging trends in spin crossover (SCO) based functional materials and devices. *Coord. Chem. Rev.* **2017**, *346*, 176−205.

(18) Kahn, O. Spin-Transition Polymers: From Molecular Materials Toward Memory Devices. *Science* **1998**, *279*, 44−48.

(19) Bao, X.; Guo, P.-H.; Liu, W.; Tucek, J.; Zhang, W.-X.; Leng, J.-D.; Chen, X.-M.; Gural'skiy, I.; Salmon, L.; Bousseksou, A.; Tong, M.-L. Remarkably high-temperature spin transition exhibited by new 2D metal-organic frameworks. *Chem. Sci.* **2012**, *3*, 1629−1633.

(20) Spek, A. L. Structure validation in chemical crystallography. *Acta Crystallogr., Sect. D: Biol. Crystallogr.* **2009**, *65*, 148−155.

(21) *Quantachrome Autosorb*, version 1.56; Quantachrome GmbH & Co. KG: Odelzhausen, Germany, 2009.

(22) Kolnaar, J. J. A.; van Dijk, G.; Kooijman, H.; Spek, A. L.; Ksenofontov, V. G.; Gütlich, P.; Haasnoot, J. G.; Reedijk, J. Synthesis, Structure, Magnetic Behavior, and Mössbauer Spectroscopy of Two New Iron(II) Spin-Transition Compounds with the Ligand 4-Isopropyl-1,2,4-triazole. X-ray Structure of Fe_3(4-isopropyl-1,2,4-triazole)$_6$(H_2O)$_6$(tosylate)$_6$.2H_2O. *Inorg. Chem.* **1997**, *36*, 2433−2440.
(23) Bancroft, G. M.; Mays, M. J.; Prater, B. E. The single line mössbauer spectrum of $[Fe(NH3)_6]^{2+}$. *Chem. Phys. Lett.* **1969**, *4*, 248−250.
(24) Asch, L.; Adloff, J. P.; Friedt, J. M.; Danon, J. Motional effects in the mössbauer spectra of iron(II) hexammines. *Chem. Phys. Lett.* **1970**, *5*, 105−108.
(25) Müller, E. W.; Spiering, H.; Gütlich, P. Spin transition in $[Fe(phen)_2(NCS)_2]$ and $[Fe(bipy)_2(NCS)_2]$: Hysteresis and effect of crystal quality. *Chem. Phys. Lett.* **1982**, *93*, 567−571.
(26) Mueller, E. W.; Spiering, H.; Guetlich, P. Effect of crystal quality on the spin-transition behavior in a cobalt(II) complex. *Inorg. Chem.* **1984**, *23*, 119−120.
(27) Haddad, M. S.; Federer, W. D.; Lynch, M. W.; Hendrickson, D. N. Spin-crossover ferric complexes: Unusual effects of grinding and doping solids. *Inorg. Chem.* **1981**, *20*, 131−139.
(28) Haddad, M. S.; Federer, W. D.; Lynch, M. W.; Hendrickson, D. N. An explanation of unusual properties of spin-crossover ferric complexes. *J. Am. Chem. Soc.* **1980**, *102*, 1468−1470.
(29) Brooker, S. Spin crossover with thermal hysteresis: Practicalities and lessons learnt. *Chem. Soc. Rev.* **2015**, *44*, 2880−2892.
(30) Muñoz Lara, F. J.; Gaspar, A. B.; Aravena, D.; Ruiz, E.; Muñoz, M. C.; Ohba, M.; Ohtani, R.; Kitagawa, S.; Real, J. A. Enhanced bistability by guest inclusion in Fe(II) spin crossover porous coordination polymers. *Chem. Commun.* **2012**, *48*, 4686−4688.
(31) Weber, B.; Bauer, W.; Obel, J. An iron(II) spin-crossover complex with a 70 K wide thermal hysteresis loop. *Angew. Chem., Int. Ed.* **2008**, *47*, 10098−10101.
(32) Gütlich, P.; Gaspar, A. B.; Garcia, Y. Spin state switching in iron coordination compounds. *Beilstein J. Org. Chem.* **2013**, *9*, 342−391.
(33) Petříček, V.; Dušek, M.; Palatinus, L. Crystallographic Computing System JANA2006: General features. *Z. Kristallogr. - Cryst. Mater.* **2014**, *229*, 229.
(34) Blum, V.; Gehrke, R.; Hanke, F.; Havu, P.; Havu, V.; Ren, X.; Reuter, K.; Scheffler, M. Ab initio molecular simulations with numeric atom-centered orbitals. *Comput. Phys. Commun.* **2009**, *180*, 2175−2196.
(35) Ren, X.; Rinke, P.; Blum, V.; Wieferink, J.; Tkatchenko, A.; Sanfilippo, A.; Reuter, K.; Scheffler, M. Resolution-of-identity approach to Hartree−Fock, hybrid density functionals, RPA, MP2 and GW with numeric atom-centered orbital basis functions. *New J. Phys.* **2012**, *14*, 53020.
(36) Havu, V.; Blum, V.; Havu, P.; Scheffler, M. Efficient integration for all-electron electronic structure calculation using numeric basis functions. *J. Comput. Phys.* **2009**, *228*, 8367−8379.
(37) Nocedal, J.; Wright, S. J. *Numerical Optimization*, 2nd ed.; Springer Series in Operations Research and Financial Engineering; Springer Science+Business Media LLC: New York, 2006.
(38) Perdew, J. P.; Ruzsinszky, A.; Csonka, G. I.; Vydrov, O. A.; Scuseria, G. E.; Constantin, L. A.; Zhou, X.; Burke, K. *Phys. Rev. Lett.* **2008**, *100*, 136406.
(39) Perdew, J. P.; Burke, K.; Ernzerhof, M. Generalized Gradient Approximation Made Simple. *Phys. Rev. Lett.* **1996**, *77*, 3865−3868.
(40) Adamo, C.; Barone, V. *J. Chem. Phys.* **1999**, *110*, 6158.